B.Y. Zhou, M. Morelli, A. Guardone, P. Dehpanah, N.R. Gauger
Aeroacoustic Analysis of a Wing-Tip Mounted Propeller Configuration
in: AIAA Aviation 2021 Forum, AIAA, 2021, ISBN: 9781624106101, p. 1-19, AIAA 2021-2224
[AIAA Aviation 2021 Forum, Virtual Event, 2-6 Aug. 2021]
doi:10.2514/6.2021-2224

Aeroacoustic Analysis of a Wing-Tip Mounted Propeller Configuration

Beckett Y. Zhou*
Department of Aerospace Engineering, University of Bristol
Queens Building, University Walk, Bristol, BS8 1TR, United Kingdom

Myles Morelli † and Alberto Guardone‡
Department of Aerospace Science and Technology, Politecnico di Milano
Building B12, Via La Masa 34, Milano, MI 20156, Italy

Payam Dehpanah§ and Nicolas R. Gauger ¶
Chair for Scientific Computing, TU Kaiserslautern
Bldg 34, Paul-Ehrlich-Strasse, 67663 Kaiserslautern, Germany

This work focuses on analysing the turbulent flow-field and noise of a wing-tip mounted propeller configuration using the model and test conditions released by the Workshop for Integrated Propeller Prediction (WIPP). In particular, the unsteady Reynolds-averaged Navier-Stokes and enhanced delayed detached eddy simulations with Spalart-Allmaras turbulence model are performed in a time-accurate manner. A multi-zone sliding mesh technique is used to allow for the relative motion of the propeller with the stationary wing. Time-averaged pressure coefficients at four spanwise locations along the wing surface are evaluated and shown to be in good agreement with the experimental data, including the two locations directly in the propeller slipstream. The simulations reveal two major noise sources of this wing-tip mounted propeller configuration, namely the turbulent wake and tip vortex generated by the propeller blades, which both impinge on the wing and nacelle surfaces as they convect downstream. Visualization of the surface pressure fluctuations at 6 different operating conditions with varying Mach number and angle-of-attack reveals the noise footprints on this integrated propeller-wing system. In particular, the impingement of propeller blade tip vortices on the leading edge of the wing towards the nacelle is identified to be the dominant noise source. This is confirmed by the farfield noise computation for observers located on the azimuthal propeller plane and the fly-over plane, which reveals that at most observer angles, especially the side-line ones, the unsteady loading on the wing and nacelle surfaces represents the dominant noise source.

I. Introduction

Propeller-driven engines have garnered renewed interest in the aircraft industry due to the emergence of electric and distributed propulsion systems. These systems, typically installed on lighter and slower vehicles, demand less engine power and attain lower blade tip speeds, allowing them to achieve 10-20% higher fuel efficiency over typical turbofan engines in static and flight test conditions.[1] This inclination has led NASA to reinstate its X-Plane series, and with this, the latest aircraft under development is the experimental X-57 plane. Throughout the research and development of this aircraft, one of the key features is the use of wing-tip mounted propellers to increase the efficiency of the aircraft.

*Lecturer in Aeroacoustics, Member AIAA, beckett.zhou@bristol.ac.uk
†Post-Doctoral Researcher, mylescarlo.morelli@polimi.it
‡Professor, alberto.guardone@polimi.it
§Research Assistant, payam.dehpanah@scicomp.uni-kl.de
¶Professor, Associate Fellow AIAA, nicolas.gauger@scicomp.uni-kl.de

A clean wing-tip produces strong three-dimensional vortical structures, so intuitively, the placement of propellers mounted on the wing-tips can help reduce the wings induced drag by attenuating the wing-tip vortex by the propeller slipstream. In the past, a major drawback of wing-tip mounted propellers has been the integration of the propeller with the airframe and the issue of having a high mass at the wing tip causing aeroelastic problems. The emergence of electric and distributed propulsion systems however increases the design flexibility by eliminating potential penalties through the down-scaling of the motors.[2]

To further understand wing-tip mounted propellers an open Workshop for Integrated Propeller Prediction (WIPP) has been established.[3] The WIPP configuration provides experimental results of an isolated wing-tip mounted propeller for numerical cross-code validation. The database allows for the assessment of important parameters to predict complex propeller-wing interactional effects and to understand the impact of the propeller on the wing's aerodynamic efficiency. A critical first stage of this work was the simulation of the aerodynamics of the WIPP configuration in order to assess the numerical prediction capabilities of the open-source SU2 solver.[4] In order to evaluate the numerical prediction capabilities, quantities including the pressure coefficient distribution along different stations of the wing and wake data were compared with measurements from the experimental database. In the main, the numerical predictions were shown to be in good agreement with the experimental measurements. Meanwhile, the strong interactional behaviour between the propeller-tip vortices and wing-tip was captured. However the study highlighted that this complex interaction between the propeller and wing is potentially a major source of noise. This leads to the second critical stage of this work, the assessment of the noise levels of wing-tip mounted propeller configurations.

An undesirable factor associated with propeller-driven engines is their noise level. While the dominant noise source in such engines is due to the unsteady aerodynamic loading on the rotating propeller blades, various installation/integration noise sources have also been shown to be significant. Depending on the propeller configuration, the interactional behaviour between either the propeller-tip vortices and wing or the turbulent wing wake and propeller may lead to significant structure-borne cabin noise.

In the past, propeller noise has primarily been studied on conventional aircraft test setups which can be categorised into either tractor and pusher propeller configurations where the propeller is mounted on a pylon. While the generation of noise is the primary concern, tractor propeller configurations have been shown to be advantageous.[5,6] The interaction between propeller-tip vortices and the downstream pylon in tractor configurations produces unsteady blade loads on the pylon and is subsequently a major source of noise.[7–9] Meanwhile in pusher configurations, the pylon wake disturbs the inflow to the propeller and this unsteady interaction is a significant source of noise.[10–12]

The issue of propeller noise on tractor configurations has recently been further investigated by researchers primarily from Delft University of Technology to address key parameters such as advance ratio and angle-of-attack on the unsteady pylon loading.[13–16] Detailed information including the time-dependent spatial distribution of pressure over the wing and the integrated effect of the unsteady pressure distribution on overall unsteady wing loading were measured and used for noise prediction. Incidentally, the propeller is positioned at the pylon tip as is the case with the WIPP configuration. However, differences include the pylon using a non-lifting NACA 0012 wing profile and a support sting which is attached to the nacelle.

It is widely recognized that for certification of propeller-driven vehicles, aeroacoustic considerations must be the central focus of the design and no longer be treated a side constraint. Therefore accurate and robust numerical tools are urgently needed by the aircraft industry to characterize, predict and more importantly optimize novel propeller-powered configurations.

Within this work, we seek to utilize the extensive and open experimental WIPP database to simulate the flow field of the full WIPP configuration. The open-source multi-physics SU2 solver[17] will be used for the validation exercise. To accurately capture the rich propeller-wing interactional flow physics the blades will be fully resolved and to allow the propeller to move in relative motion to the wing a sliding mesh technique will be used. In so doing, we aim to elucidate the key noise generation mechanisms and visualize the noise footprint both on the propeller and wing surfaces. The final goal of the work is to predict the farfield noise of the WIPP configuration and identify the major noise sources at an individual component level.

The organization of this work is as follows. In Section II, the WIPP model, as well as the test conditions are described. In Section III, the multi-physics SU2 solver and computational aeroacoustic framework are presented. Section IV presents the SU2 simulation results of the flow-field and noise generation. Finally, the conclusions and outlook for future work are discussed in Section V.

II. WIPP Model Description

The computational test case replicates the WIPP experiment of a wing-tip mounted propeller, as shown on Figure 1. The test took place in the Lockheed Martin Low-Speed Wind Tunnel (LSWT) in Marietta, Georgia, USA as part of the NASA/Armstrong X-57 research program. The WIPP model was designed by Mark Skeehan at Lockheed Martin Aeronautical Systems and was fabricated by Empirical Systems Aerospace (ESAero). The WIPP model is a 40.5%-scale semi-span model of the X-57, specifically designed to allow it to be mounted onto the LSWT external balance. The model is positioned vertically and incorporates a non-metric boundary layer splitter plate which is mounted to the LSWT external balance. The span of the wing relative to the wind tunnel floor is 67.065 inches. The wing has a taper ratio of 0.7 and an aspect ratio of 6.7. The chord of the wing at its root is 11.6 inches and the chord of the wing at its tip is 8.6 inches. The mean aerodynamic chord of the wing can then be considered as 10.15 inches. The wing also contains a slight leading-edge sweep of 1.9°. The model uses a four-bladed propeller system based on an already available 10%-scale C-130 model. The propeller diameter is 16.2 inches. The propeller blades are calibrated for a 38° pitch at the root and have a significant negative twist from the root to the tips of the blades. The propeller is mounted onto a nacelle at the wing tip. The nacelle is 24.15 inches long and has a maximum diameter of 4.75 inches at its center before being tapered and rounded at the leading and trailing edges.

To measure the interactional effect of the propeller on the wing, the model was instrumented with a total of 96 static pressure taps which were located at six different wing spanwise locations. These spanwise locations were 34, 44, 54, 57, 60.75 and 63 inches from the wind tunnel floor. Each of these spanwise sections then contained 10 static pressure taps on the upper surface and 6 static pressure taps on the lower surface. Wake data also captured the flow-field behind the propeller, nacelle and wing during the experiment using a wake survey system. This system used a wake rake which contained a total of twelve 7-hole pressure probes mounted on a strut 3.0 inches apart.

The tests were then conducted at a variety of Mach numbers, thrust coefficients, and angles-of-attack. The flight speeds investigated were Mach 0.04, 0.08, and 0.11. To achieve variations in the thrust coefficient, the rotational speed of the model propeller was altered. The thrust coefficients investigated ranged from $C_T = 0 \rightarrow 0.40$. There were then three different angle-of-attack schedules planned termed A1, A2, and A3 which ranged from -10 $\rightarrow$ +20 degrees.

Various experimental configurations were also tested for the calibration of the instrumentation, for the assessment of the effectiveness of the ailerons during flow separation, and for determining the influence of the propeller on the performance of the wing. The configurations tested hence included an empty wind tunnel with the model removed, an isolated wing, and an integrated wing and propeller. In total 198 test runs were completed.

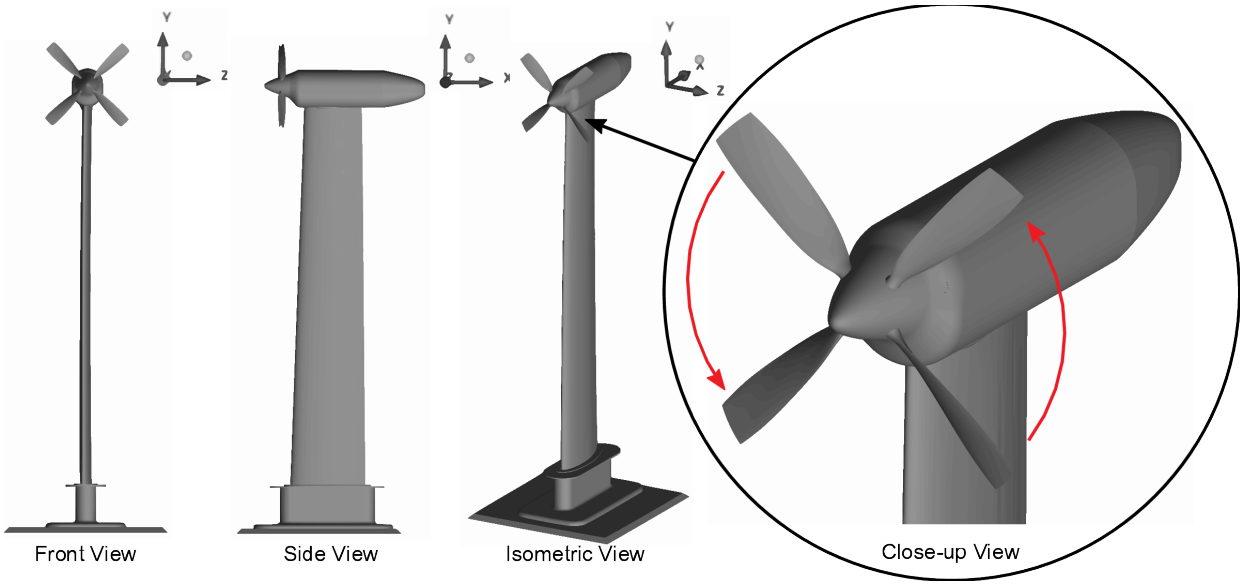

Figure 1: The wing-tip mounted propeller configuration

III. Prediction Analysis Methodologies

III.A. Turbulent Flow Simulation

The SU2 open-source software suite was specifically developed for solving problems governed by partial differential equations (PDEs) and PDE-constrained optimization problems. It was developed with the aerodynamic shape optimization problems in mind. Therefore the suite is centered around a Reynolds-averaged Navier-Stokes (RANS) solver capable of simulating compressible, turbulent flows commonly found in problems in aerospace engineering. The governing equations are spatially discretized using the finite volume method, on unstructured meshes. A number of convective fluxes discretization schemes have been implemented, such as the Jameson-Schimdt-Turkel (JST) scheme and the upwind Roe scheme. The turbulence can be either modeled by the Spalart-Allmaras(S-A) model or the Menter Shear Stress Transport (SST) Model. For unsteady flows, a second-order dual time-stepping method can be used to obtain time-accurate solutions.

For scale-resolving capabilities, the enhance delayed detached eddy simulation (EDDES) based on the S-A model was implemented in SU2 by Molina[18] and has been demonstrated to successfully predict separated flows.[19,20] To mitigate the "grey area" problem characterized by slow transition from RANS to LES mode in the shear-layer, a shear-layer adapted (SLA) sub-grid scale model[21] was implemented. In addition, to limit the numerical dissipation in LES part of the EDDES model, the inviscid flux is computed using the so-called simple low dissipation advection upstream (SLAU2).[22]

III.B. Noise Simulation

Acoustic prediction is achieved using Farassat's Formulation-1A (F1A) of the Ffowcs Williams and Hawkings (FW-H) equations.[23] This F1A formulation has been implemented in the SU2 suite[24,25] and computes the far-field noise from surface pressure fluctuations extracted from a preceding unsteady flow simulation. The F1A equation to be solved for the FW-H analogy is as follows;

$$p'(\boldsymbol{x},t) = p'_T(\boldsymbol{x},t) + p'_L(\boldsymbol{x},t) \tag{1}$$

where the thickness and loading noise contributions are respectively given by $p'_T(\boldsymbol{x},t)$ and $p'_L(\boldsymbol{x},t)$. For an arbitrary observer distance, the thickness and loading terms in Eq. 1 can then be written in a computationally feasible way as presented by Di Francescantonio,[26]

$$p'_T(\boldsymbol{x},t) = \frac{1}{4\pi}\int_S \left[\frac{\rho_0\left(\dot{U}_i n_i + U_i \dot{n}_i\right)}{r\left|1-M_r\right|^2}\right]_{\text{ret}} \mathrm{d}S + \frac{1}{4\pi}\int_S \left[\frac{\rho_0 U_i n_i K}{r^2\left|1-M_r\right|^3}\right]_{\text{ret}} \mathrm{d}S \tag{2}$$

and

$$p'_L(\boldsymbol{x},t) = \frac{1}{4\pi c}\int_S \left[\frac{\dot{F}_i \hat{r}_i}{r\left|1-M_r\right|^2}\right]_{\text{ret}} \mathrm{d}S + \frac{1}{4\pi}\int_S \left[\frac{F_i \hat{r}_i - F_i M_i}{r^2\left|1-M_r\right|^2}\right]_{\text{ret}} \mathrm{d}S + \frac{1}{4\pi c}\int_S \left[\frac{F_i \hat{r}_i K}{r^2\left|1-M_r\right|^3}\right]_{\text{ret}} \mathrm{d}S \tag{3}$$

where the definition of each symbol is discussed in its entirety in Ref.[26] A key aspect of this formulation is that the time derivatives are moved inside the integrals. As a result, this means it does not require any numerical evaluation of derivatives of quantities depending on the retarded time.

IV. Results

IV.A. Test Conditions

The aerodynamic simulation results of the WIPP wind tunnel test are based on the fully integrated wing and propeller configuration. Run numbers 33 and 80 of the experimental database were used for the validation of the flow field. The test conditions from run number 33 and 80 are shown in Table 1. The experimental results from run number 33 contain the surface pressure data along the spanwise direction of the wing and the experimental results from run number 80 contain the wake survey data. The α schedule used within this run was A3 where the angle-of-attack ranged from -10 $\rightarrow$ +20 degrees. The flight speed of this run was the highest tested in the LSWT at Mach = 0.11. The wind tunnel freestream pressure, at this flight speed was recorded and measured as Q = 18.31 lbf/ft^2. The mean aerodynamic chord of the wing was used as the reference length for computing the Reynolds number of flow field and was computed to be Re = 0.660×10^6. The propellers were approximately rotating at 8000RPM to achieve a thrust coefficient of $C_T = 0.4$.

Table 1: Aerodynamic Configuration and Parameters.

Configuration	α Schedule	Mach [-]	Q [lbf/ft^2]	Re [-]	C_T [-]	Run No
Integrated Wing and Propeller	A3	0.11	18.31	0.660×10^6	0.4	33, 80

In addition to the test conditions setup for the validation of the flow field, a further set of conditions are selected for the noise prediction and are shown in Table 2. In particular, the influence of the flight speed and angle-of-attack are assessed. Simulations at two different flight speeds, Mach = 0.08, 0.11 and three different angles-of-attack, $\alpha = 0^\circ, 5^\circ, 15^\circ$ are conducted which gives rise to a 2×3 test matrix. Therefore the noise level of the WIPP configuration is evaluated at 6 different operating points. The baseline operating condition is considered as M011AoA00 due to this corresponding to the conditions from Table 1 which are used for the flow-field validation.

Table 2: Acoustic Test Matrix.

Acronym	Mach [-]	α [$^\circ$]
M008AoA00	0.08	0
M008AoA05	0.08	5
M008AoA15	0.08	15
M011AoA00	0.11	0
M011AoA05	0.11	5
M011AoA15	0.11	15

IV.B. Mesh Generation

The simulation of propeller-wing interactions are rich in flow physics and so require a high fidelity of computational modeling. Thus, to allow the propeller to move in relative motion to the wing the numerical discretization of the mesh is required. Within this work, a sliding mesh technique is used to allow the propeller to rotate while the wing remains stationary. The numerical discretization of the mesh used within this work is shown in Fig. 2 and shows the cylindrical cut-out where the propeller is positioned. The mesh is hereafter considered as a multi-zone problem where the external stationary zone and the internal rotating internal zone are considered as separate entities and a nearest-neighbour interpolation technique is used for data exchange between the zone interfaces.

To simplify the generation of the mesh, the clamp at the base of the wing was not considered since there was no pressure tap measurements and wake data collected this close to the root of the wing. An artificial wall was then introduced into the simulation where the root of the wing meets the external balance at $y = 7.115$ in. using euler boundary conditions to avoid the need of modelling the boundary layer of the artificial wind tunnel floor. The leading edge of the nacelle was also reconstructed in order to insert the sliding mesh surface interfaces. With the reduction in the length of the nacelle being only slight and with there being no wake data recorded in this region due to it being too close to the propeller this assumption was justified. Artificial wind tunnel inflow and outflow walls were placed at 25 propeller radii upstream and downstream of the model propeller and wing at $x = \pm 25$R. Wind tunnel walls were also placed above the model at $y = 15$R and either side of the model at $z = \pm 10$R.

The stationary zone containing the wing and nacelle consists of mixed quadrilateral and triangular surface elements elements. The rotating propeller surface mesh uses triangular elements. The boundary layer of the wing, nacelle and propeller is sufficiently resolved to ensure $y^+ < 1$. Tetrahedral volume elements are used outside of the boundary layer. The rotating internal boundary interface and stationary external boundary interface both use entirely triangular surface elements.

A prerequisite for accurate wake modeling of the WIPP configuration is a high-quality and high resolution mesh in the region behind the propeller to preserve the main blade-tip vortices and smaller scale vortex structures. Suitable refinement is important to reduce numerical dissipation of the wake so that blade-tip vortex/wing interaction effects are correctly modeled. The importance of the mesh refinement region in the near-field propeller wake around the nacelle was previously presented by Zhou et al.[4] Based on this work, details of the grid selected for this study are outlined in Table 3.

The naming convention of the grid is maintained to be consistent with the previous work. The grid outlined in

Table 3: Details of the three levels of grid refinement.

Name	No. Volume Elements			Wake Element Size*	Density Region
	Propeller	Wing	Total	(l/c_{tip})	
Grid-03 (G3)	12.3M	52.6M	64.9M	0.0682	Yes

* cell edge length l non-dimensionalized by blade tip chord c_{tip}, measured at a distance $0.5R_{\text{prop}}$ behind the tip of the propeller.

Table 3 is shown in Fig. 2. There are 12.3M elements in the internal propeller zone and 52.6M elements in the external wing zone. In total, the combined number of elements across both zones is 64.9M. It has a maximum surface element size of 0.002m which expand at a ratio of 1.1 away from the surface. Increasing the expansion ratio allowed for points with minimal influence, such as close to the wing root where there is no measured wake data, to be redistributed elsewhere. A local density region was then placed around the nacelle and propeller wake with a maximum element size of 0.003m in this region Fig. 2a. The distribution of elements in the near-field wake region is shown more closely in Figs. 2b & 2c.

IV.C. Aerodynamic Prediction

The simulations are performed with both unsteady RANS and hybrid RANS/LES scale resolving capabilities. A total of 15 propeller revolutions are simulated. The flow statistics are computed over the last 10 revolutions. The physical time step is $2.1 \times 10^{-5} s$ which is equivalent to 1° of revolution per time step at approximately 8000RPM.

The static pressure tap measurements recorded during run number 33 are used for validation of the chordwise pressure coefficient distribution along spanwise sections of the wing. The conditions simulating $M_{\infty} = 0.11$ corresponds to the highest dynamic pressure obtained throughout the experimental test campaign. The numerical results of the mean pressure coefficient at four different spanwise locations along the wing are shown in Fig. 3. Pressure tap location $y = 54.386$ in. is outwith the propeller slipstream. Pressure tap location $y = 57.386$ in. is aligned approximately 1.5 in. outward of the propeller tip. Pressure tap locations at $y = 60.955$ in. and $y = 63.469$ in. are directly in the propeller slipstream. The results shown begin close to the root of the wing and progressively get closer towards the tip of the wing. Time-averaged URANS-SA predictions are used for comparison with experimental data. The predicted pressure coefficient distributions at the spanwise location outwith the propeller wake is in close agreement with the measured data and is shown in Fig. 3a. The predicted pressure coefficient distribution at the spanwise location which corresponds to being marginally outward of the blade tip is shown in Fig. 3b. It illustrates that the pressure tap is beyond the wake of the propeller which the prediction captures. The predicted pressure coefficient distributions at the spanwise locations inside the propeller slipstream are shown in Fig. 3c & 3d. The interaction effects of the propeller slipstream at these spanwise locations are shown to have a significant influence on the pressure coefficient distributions, leading to a clear suction peak near the wing leading edge on the blade retreating side. This dynamic effect is more challenging to simulate and accurately model however the blade-tip vortex disturbances on the surface of the wing appear to well represented. Overall, the computed pressure coefficient is in good agreement with the measured data from run number 33. This close agreement is particularly true for the results outwith the influence of the propeller. As the influence of the propeller becomes apparent slight discrepancies arise, however despite this, the suction peak is well captured.

To help visualize the highly three-dimensional nature of the problem the Q-criterion colored by dimensionless streamwise velocity is shown in Figs. 4a & 4b for the URANS-SA simulations and in Figs. 4c & 4d for the EDDES-SA simulations. The vortical structures are preserved and persist further downstream. In addition, the EDDES simulations further resolve smaller turbulence structures in the wake region compared to their URANS counterparts. The EDDES-SA simulation on G3 clearly reveals two major interactional noise sources: the turbulent wake and tip vortex generated by the propeller blades, both impinging upon the wing and nacelle surfaces as they convect downstream. In addition, the secondary vortex emanating from the trailing edge of the blade tip is also captured. It is this interactional behaviour close to the propeller which influences the pressure coefficient on the wing displayed in Fig. 3c & 3d.

In light of the promising aerodynamic results, progression towards the prediction of the aeroacoustics was the subsequent area of interest. As a first step in assessing the noise sources in this integrated wing-propeller configuration, the instantaneous pressure fluctuations over the full configuration captured by URANS and EDDES simulations on G3 are shown in Fig. 5. The locations at which the blade-tip vortices impact on the wing and nacelle correlate into strong noise sources, as evidenced by the alternating pressure fluctuation patterns near the wing-tip below the nacelle. In

addition, the turbulent wake shed by the propeller blades leaves spiralling patterns around the nacelle surface. EDDES appears to capture the finer features of the surface pressure fluctuation patterns much more clearly, especially around the nacelle.

The surface 'noise footprint' is visualized by the root-mean-square (RMS) of the pressure fluctuation and shown in Fig. 6. The dominant noise source is located at the leading edge of the wing immediately below the nacelle where the tip vortex in the propeller slipstream makes first contact with the wing surface. This is consistent with the findings of Avallone et al. in their computational aeroacoustic study of a similar configuration.[16] From a noise reduction perspective, this indicate that in addition to optimizing the shape of the blades, it may also be highly effective to consider also optimally morphing the leading edge of the wing in the slipstream.

EDDES-SA simulations are performed for the remaining five operating conditions listed in Table 2 to further analyse the noise. The instantaneous and RMS of pressure fluctuation of all six cases, viewed from the blade advancing side (below the airframe) are compared in Fig. 7 and Fig. 8 respectively. It is observed that the at all ranges of AoA, a lower flight Mach number leads to more intense impingement patterns on wing and nacelle surfaces as highlighted in Fig. 7. This is likely to be due to the propeller-tip vortices remaining within the vicinity of the wing for a longer period of time. Meanwhile, Fig. 8 shows that for the higher Mach number of $M_\infty = 0.11$, there is a noticeable decrease on surface noise footprint on the wing and nacelle as AoA is increased to 15 deg. This observation is likely due to the propeller-tip vortices being convected away from the wing quicker decreasing their strength and therefore influence on the wing and nacelle.

IV.D. Acoustic Analysis

Farfield noise directivities are computed for the six operating conditions listed in Table 2 using the solid-surface FWH solver outlined in Section III.B. Each acoustic simulation is assessed on two different planes: the azimuthal propeller plane at $x/D = 0$ and the fly-over plane at $y/D = 0$. The analysis of the results on the azimuthal propeller plane are shown in Fig. 9, while the results from the fly-over plane are shown in Fig. 10. The observers are located at a distance of $10D$ from the center of the propeller. For each plane, the individual propeller-spinner and wing-nacelle contributions to the overall sound pressure level (OASPL) are displayed. In addition, the combined OASPL due to all surfaces are shown.

The azimuthal propeller plane directivity displayed in Fig. 9 shows that the propeller-spinner contribution resembles a distorted monopole, while the wing-nacelle contribution resembles a dipole symmetric about the plane of the wing. At both Mach numbers, as the AoA is increased, the propeller monopole becomes more distorted with heightened noise levels at all observer angles below the propeller-wing configuration. Furthermore, at a given AoA, the propeller noise is 1-2dB stronger at the lower Mach number of $M_\infty = 0.08$. This is due to the larger extent of leading edge flow separation on the propeller blades operating at lower Mach number, as shown in Fig. 11. As the flight Mach number is reduced from 0.11 to 0.08, the blade pitch is not changed, resulting in a higher relative AoA the blade sees at lower Mach number. Consequently, the flow separation on the propeller blades is more extensive at lower Mach number. This is commonly encountered for propellers with sharp leading edges operating at low speeds during takeoff and landing. For $M_\infty = 0.11$, as the AoA increases, the wing-nacelle noise component is reduced. This is in line with the observations from the surface noise footprint which can be seen in Fig. 8. The symmetry of the wing-nacelle dipole is also lost at higher AoA. However, at lower Mach number of 0.08, these trends are not observed. At many observer angles, the unsteady loading on the wing and nacelle surfaces appear to be the dominant noise source. In particular, on the fly-over plane as shown in Fig. 10. This observation is consistent with the findings from a recent NASA study on inboard propeller-wing configuration by Zawodny et al.,[9] despite the different mounting position of the propeller relative to the wing. The pattern of the combined OASPL due to all surfaces as shown in Fig. 9e & 9f is rather nuanced, as the noise signals from the propeller-spinner and wing-nacelle surfaces are in/out of phase at different observer angles. In general, at most observer angles below the airframe, the OASPL of the full propeller-wing configuration rises as the AoA is increased.

The noise spectra for the six operating conditions are evaluated at three observer angles, $\theta = 210^\circ$, 270° & 330°, on the fly-over plane and are shown in Fig. 12. The blade-passing frequency of, $f_{\mathrm{BPF}} = 533Hz$, and higher harmonics are accurately captured in all cases. The noise spectra are similar at the two lower AoA. At AoA $= 15^\circ$, the noise spectra exhibit a significant increase in low frequency range at, $f < 250Hz$, due to significant flow separation from the wing. It is clear that the noise due to flow separation is much weaker than the tonal noise due to the rotating propeller blades and unsteady loading on the wing and nacelle surfaces.

V. Conclusion

In this work, we simulate the turbulent flow field and noise around a wing-tip mounted propeller configuration using the model and test conditions released by the Workshop for Integrated Propeller Prediction (WIPP). In particular, the unsteady RANS equations with Spalart-Allmaras turbulence model (URANS-SA) are solved in a time-accurate manner with the multi-zone sliding mesh technique in which the propeller is allowed to rotate while the wing and the nacelle remain stationary. In addition, enhanced delayed detached eddy simulations based on the Spalart-Allmaras model (EDDES-SA) are performed on the finer grids in an attempt to better resolve the turbulent wake behind the propeller.

Time-averaged pressure coefficients at four spanwise locations along the wing surface are shown to be in good agreement with the experimental data. The two locations in the propeller slipstream in particular closely resemble the measurements and capture the blade-wing interaction effects. The Q-criterion iso-surface helps visualize the vortical structures produced by the propeller blades and assess how they interact with wing and nacelle surfaces as they are convected downstream. Furthermore, aeroacoustic aspects of this configuration at various operating conditions are also studied in the current work. The influence of the Mach number and angle-of-attack on the noise are the preliminary operating conditions assessed. Visualization of the surface pressure fluctuations reveals the noise footprints on this integrated propeller-wing system. In particular, the impingement of propeller blade tip vortices on the leading edge of the wing immediately below the nacelle is identified to be the main noise source. The farfield overall sound pressure level reveals that at many observer angles, especially the side-line, the unsteady loading on the wing and nacelle surfaces is the dominant noise source.

Looking ahead, we intend to improve the mesh resolution in the propeller wake region around the nacelle to approximately 150M elements and reduce the physical time-step to 0.25° of revolution per time step to ensure an even higher resolution of the fine-grained vortical structures for the EDDES simulation. We would also like to assess addition conditions at other Mach numbers, propeller thrust settings and angle of attacks specified by the WIPP workshop and compare our predictions with available experimental data. It must be noted that there is a glaring lack of high quality noise measurement data for wing-tip mounted propellers and installed propeller configurations in general. To advance the understanding of UAM noise and enhance the capability to control it, high-fidelity numerical simulations and experiments should be conducted in tandem. To that end, the establishment of the UAM counterpart of a 'common research model' may be of value to the community.

Finally, we intend to perform two adjoint-based shape optimizations – the first to maximize the aerodynamic efficiency of the integrated wing-propeller system and the second to minimize the far-field noise while maintaining the baseline aerodynamic performance. The shapes of the propeller blades as well as the region of the wing surface in the propeller slipstream will be optimized.

VI. Acknowledgements

The computational resources provided by the RHRK high performance computing center via the 'Elwetritsch' high performance cluster at the TU Kaiserslautern is gratefully acknowledged. The work from Politecnico di Milano would like to acknowledge receiving funding from the European Union's H2020 research and innovation programme under the Marie Skłodowska-Curie grant agreement No 721920. Further information can be found at the Network for Innovative Training on ROtorcraft Safety (NITROS) project website.

References

[1]Mann, S. and Stuart, C., "Advanced propulsion through the 1990s – an airframer's view," *21st Joint Propulsion Conference, AIAA 1985-1192*, 1985.

[2]Moore, M. D., "Misconceptions of electric aircraft and their emerging aviation markets," *52nd Aerospace Sciences Meeting*, 2014, p. 0535.

[3]Hooker, J. R., Wick, A., Ginn, S. R., Walker, J., and Schiltgen, B. T., "Overview of Low Speed Wind Tunnel Testing Conducted on a Wingtip Mounted Propeller for the Workshop for Integrated Propeller Prediction," *Special Session: Aerodynamics and Performance of Integrated Propellers I, AIAA Aviation Forum*, Reno, Nevada, US, 15-19 June, 2020, p. 2673.

[4]Zhou, B. Y., Morelli, M., Gauger, N. R., and Guardone, A., "Simulation and Sensitivity Analysis of a Wing-Tip Mounted Propeller Configuration from the Workshop for Integrated Propeller Prediction (WIPP)," *Special Session: Aerodynamics and Performance of Integrated Propellers II, AIAA Aviation Forum*, Reno, Nevada, US, 15-19 June, 2020, p. 2683.

[5]Magliozzi, B., "Noise characteristics of model counter-rotating Prop-Fans," *AIAA 11th Aeroacoustics Conference*, Sunnyvale, California, US, 19-21 October, 1987, p. 2656.

[6]Eret, P., Kennedy, J., Amoroso, F., Castellini, P., and Bennett, G. J., "Experimental observations of an installed-on-pylon contra-rotating open rotor with equal blade number in pusher and tractor configuration," *International Journal of Aeroacoustics*, Vol. 15, No. 1-2, 2016, pp. 228–249.

[7]Ljunggren, S., Samuelsson, I., and Widing, K., "Slipstream-induced pressure fluctuations on a wing panel," *Journal of aircraft*, Vol. 26, No. 10, 1989, pp. 914–919.

[8]Johnston, R. and Sullivan, J., "Unsteady wing surface pressures in the wake of a propeller," *Journal of aircraft*, Vol. 30, No. 5, 1993, pp. 644–651.

[9]Zawodny, N. S., Boyd, D. D., and Nark, D. M., "Aerodynamic and Acoustic Interactions Associated with Inboard Propeller-Wing Configurations," *AIAA Scitech 2021 Forum*, Virtual Event, 11–15 & 19–21 January 2021, p. 0714.

[10]Block, P. and Gentry Jr, C., "Directivity and Trends of Noise Generated by a Propeller in a Wake," Technical Report 2609, National Aeronautics and Space Administration, Langley Research Center, Hampton, Virginia, US, September, 1986.

[11]Block, P., "The effects of installation on single-and counter-rotation propeller noise," *9th Aeroacoustics Conference*, Williamsburg, Virginia, US, 10-15 October, 1984, p. 2263, https://doi.org/10.2514/6.1984-2263.

[12]Block, P., "Experimental Study of the Effects of Installation on Single-and Counter-Rotation Propeller Noise," Technical Report 2541, National Aeronautics and Space Administration, Langley Research Center, Hampton, Virginia, US, April, 1986.

[13]de Vries, R., Sinnige, T., Della Corte, B., Avallone, F., Ragni, D., Eitelberg, G., and Veldhuis, L. L., "Tractor propeller-pylon interaction, part I: characterization of unsteady pylon loading," *55th AIAA Aerospace Sciences Meeting, Session: Aeroacoustics - Fan Noise, Open Rotor*, Grapevine, Texas, USA, 9-13 January, 2017, p. 1175.

[14]Sinnige, T., de Vries, R., Corte, B. D., Avallone, F., Ragni, D., Eitelberg, G., and Veldhuis, L. L., "Unsteady pylon loading caused by propeller-slipstream impingement for tip-mounted propellers," *Journal of Aircraft*, Vol. 55, No. 4, 2018, pp. 1605–1618.

[15]Della Corte, B., Sinnige, T., de Vries, R., Avallone, F., Ragni, D., Eitelberg, G., and Veldhuis, L. L., "Tractor propeller-pylon interaction, part II: mitigation of unsteady pylon loading by application of leading-edge porosity," *55th AIAA Aerospace Sciences Meeting, Session: Aeroacoustics - Fan Noise, Open Rotor*, Grapevine, Texas, 9-13 January, 2017, p. 1176.

[16]Avallone, F., Casalino, D., and Ragni, D., "Impingement of a propeller-slipstream on a leading edge with a flow-permeable insert: A computational aeroacoustic study," *International Journal of Aeroacoustics*, Vol. 17, No. 6-8, 2018, pp. 1–25.

[17]Economon, T. D., Palacios, F., Copeland, S. R., Lukaczyk, T. W., and Alonso, J. J., "SU2: An open-source suite for multiphysics simulation and design," *Aiaa Journal*, Vol. 54, No. 3, 2015, pp. 828–846.

[18]Molina, E., *Detached Eddy Simulation in SU2*, Ph.d. thesis, Aeronautical Institute of Technology, 2015.

[19]Molina, E. M., Zhou, B. Y., Alonso, J. J., Righi, M., and da Silva, R. G., "Flow and Noise Predictions Around Tandem Cylinders using DDES approach with SU2," AIAA-2019-0326, 2019.

[20]Molina, E. S., Silva, D. M., Broeren, A. P., Righi, M., and Alonso, J. J., "Application of DDES to Iced Airfoil in Stanford University Unstructured (SU2)," *Progress in Hybrid RANS-LES Modelling*, edited by Y. Hoarau, S.-H. Peng, D. Schwamborn, A. Revell, and C. Mockett, Springer International Publishing, Cham, 2020, pp. 283–293.

[21]Shur, M. L., Spalart, P. R., Strelets, M. K., and Travin, A. K., "An Enhanced Version of DES with Rapid Transition from RANS to LES in Separated Flows," *Flow, Turbulence and Combustion*, Vol. 95, No. 4, 2015, pp. 709–737.

[22]Kitamura, K. and Hashimoto, A., "Reduced Dissipation AUSM-family Fluxes: HR-SLAU2 and HR-AUSM+-up for High Resolution Unsteady Flow Simulations," *Computers & Fluids*, Vol. 126, 2016, pp. 41–57.

[23]Farassat, F., "Derivation of Formulations 1 and 1A of Farassat," *NASA/TM-2007-214853. NASA Langley Research Center*, 2007.

[24]Zhou, B. Y., Albring, T., Gauger, N. R., Ilario, C. R., Economon, T. D., and Alonso, J. J., "Reduction of Airframe Noise Components Using a Discrete Adjoint Approach," AIAA-2017-3658, 2017.

[25]Icke, R. O., Baysal, O., Moy, A., Lopes, L., Zhou, B. Y., and Diskin, B., "Toward Adjoint-Based Aeroacoustic Optimization for Propeller and Rotorcraft Applications," *AVIATION 2020 Forum, AIAA-2020-3140*, 2020.

[26]Di Francescantonio, P., "A new boundary integral formulation for the prediction of sound radiation," *Journal of Sound and Vibration*, Vol. 202, No. 4, 1997, pp. 491–509.

Figures

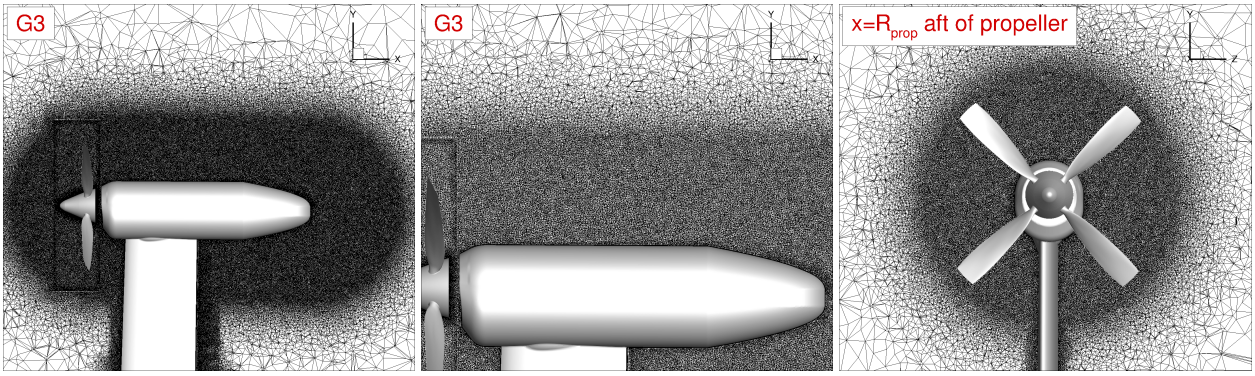

(a) Grid-03 at $z = 0$ in. (b) Near-field wake refinement. (c) $x = R_{\text{prop}}$.

Figure 2: Spatial resolution of the grids Grid-03 used for the acoustic analysis. Displaying the distribution of nodes surrounding the nacelle and near-field wake region.

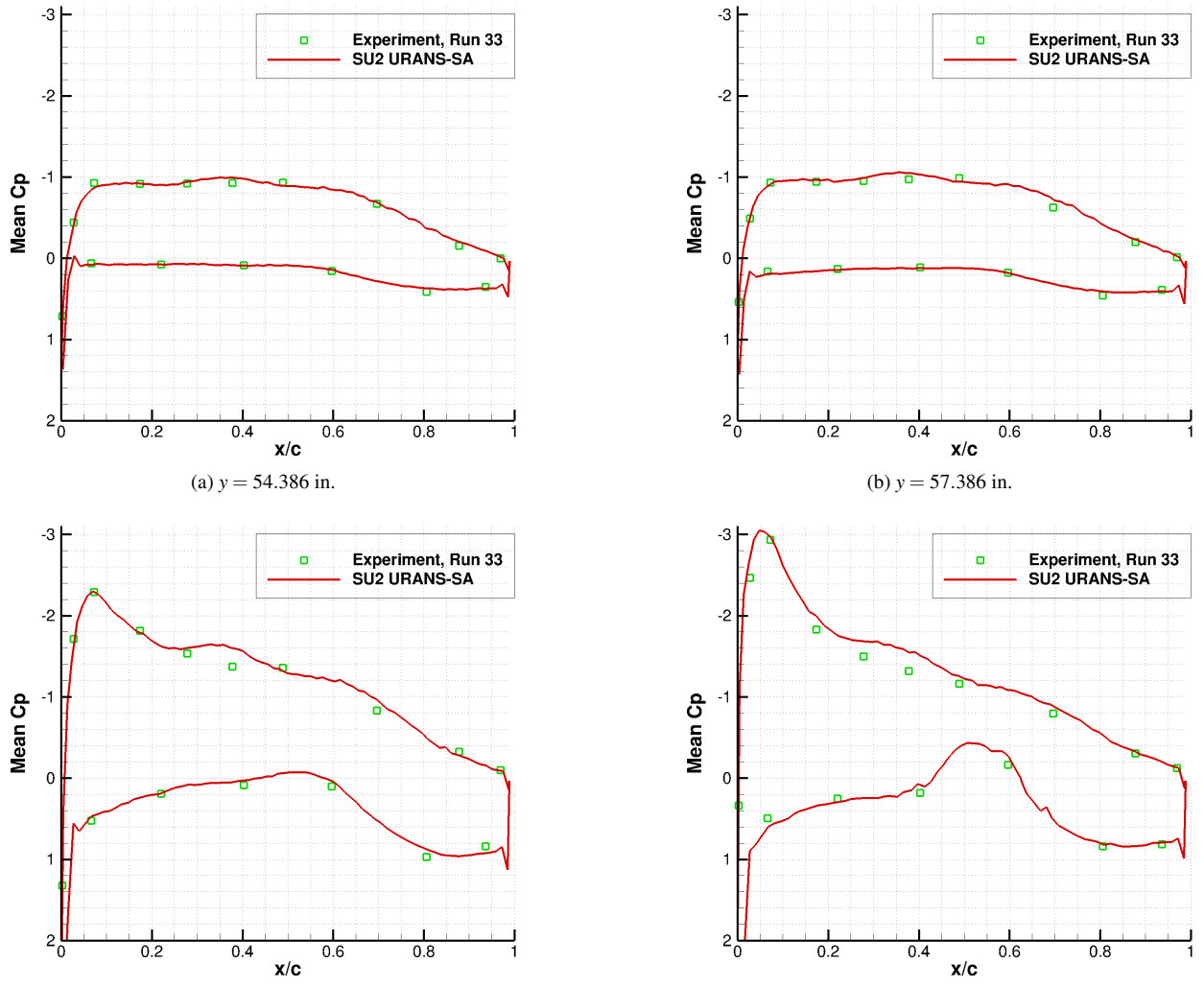

(a) $y = 54.386$ in. (b) $y = 57.386$ in.

(c) $y = 60.955$ in. (d) $y = 63.469$ in.

Figure 3: Mean pressure coefficient at four spanwise stations along the wing, $M_\infty = 0.11$, $C_T = 0.40$, $AoA = 0°$.

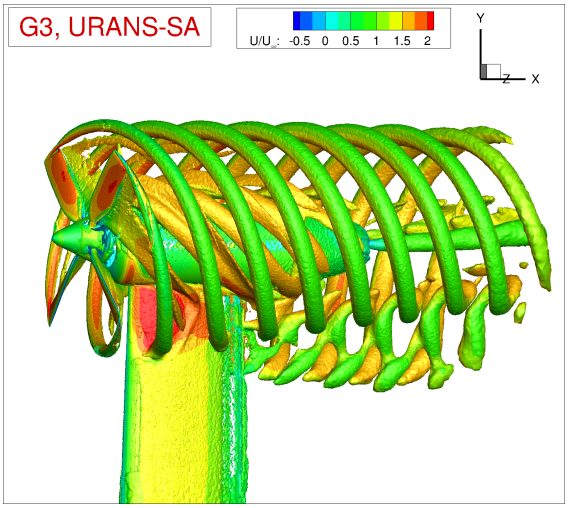

(a) URANS-SA R.

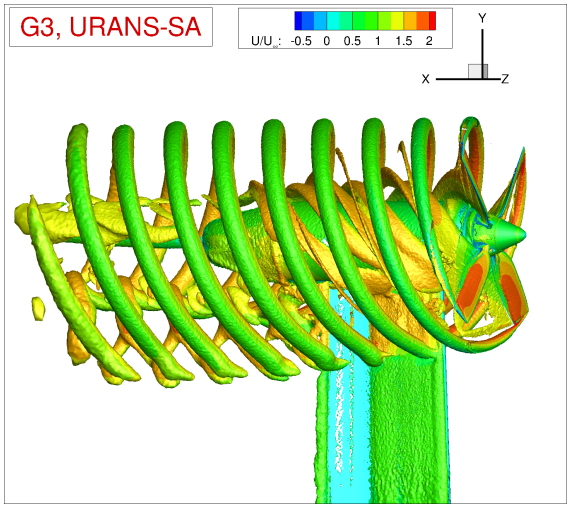

(b) URANS-SA A.

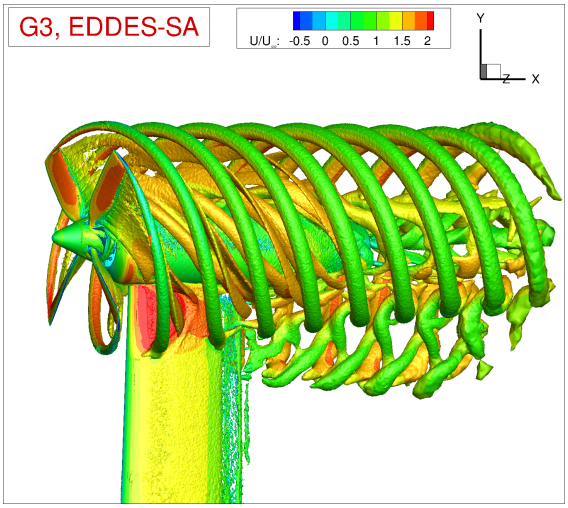

(c) EDDES-SA R.

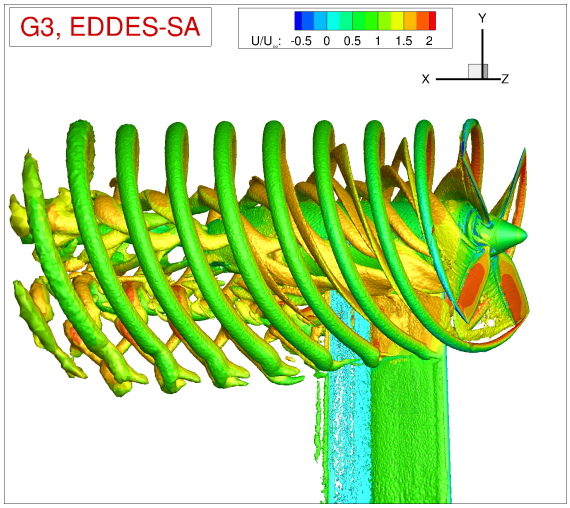

(d) EDDES-SA A.

Figure 4: Q-criterion iso-surface colored by the dimensionless streamwise velocity computed by URANS-SA and EDDES-SA on Grid-03, $M_\infty = 0.11$, $C_T = 0.40$, $AoA = 0^\circ$.

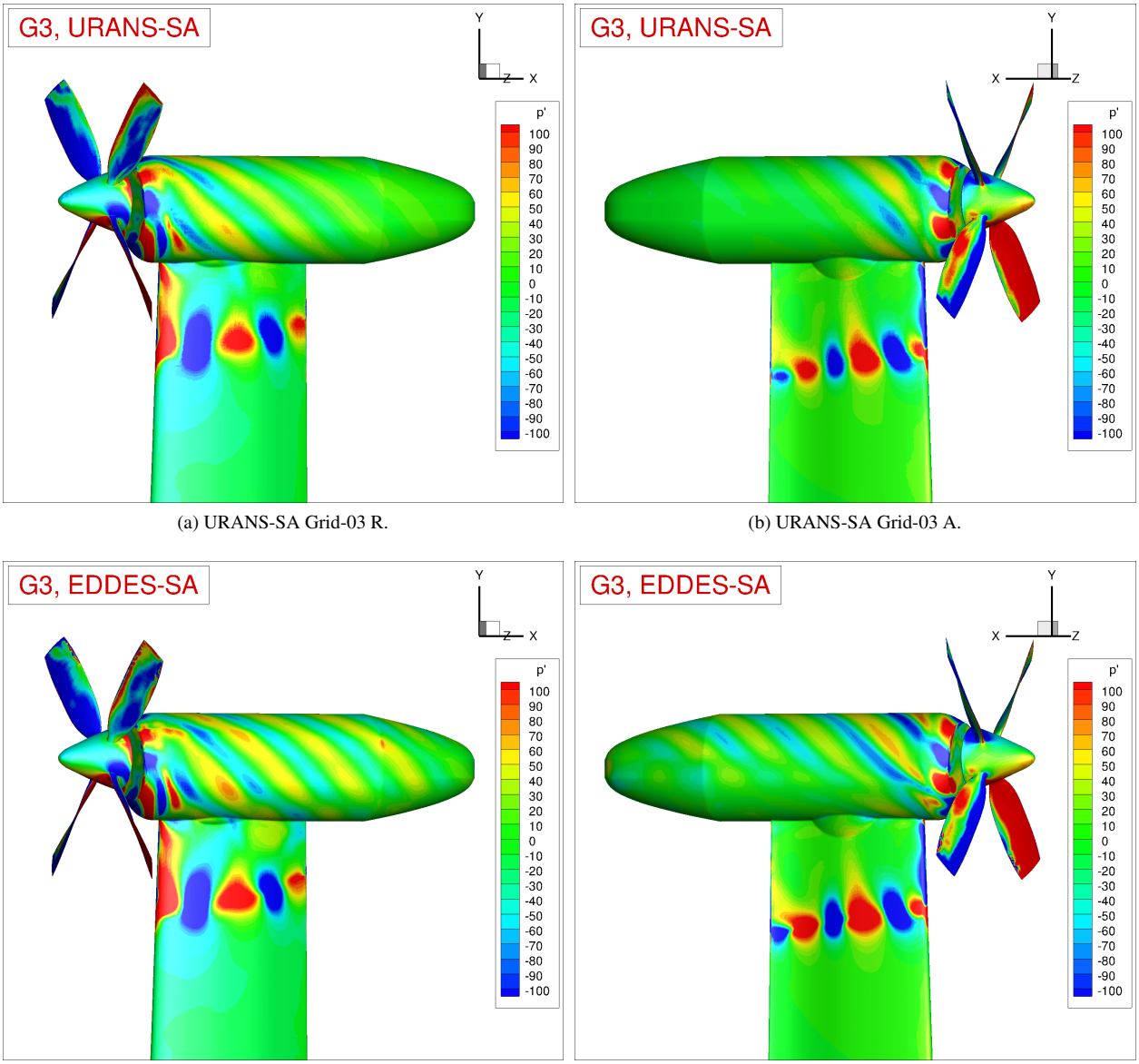

(a) URANS-SA Grid-03 R.

(b) URANS-SA Grid-03 A.

(c) EDDES-SA Grid-03 R.

(d) EDDES-SA Grid-03 A.

Figure 5: Instantaneous pressure fluctuation computed by URANS-SA and EDDES-SA on Grid-03, $M_\infty = 0.11$, $C_T = 0.40$, $AoA = 0°$.

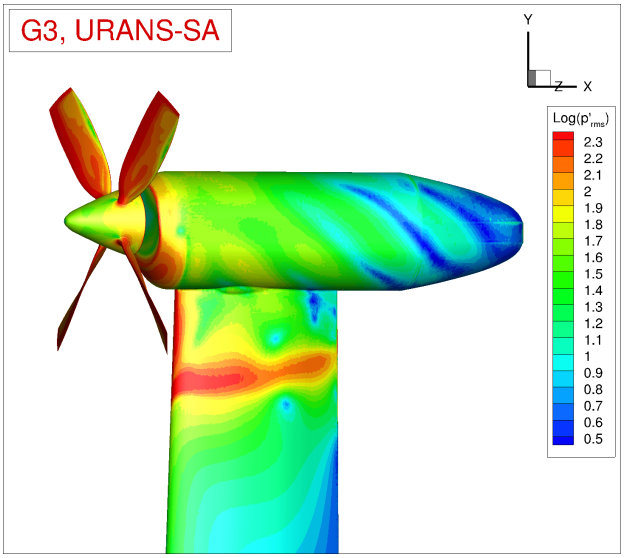

(a) URANS-SA Grid-03 R.

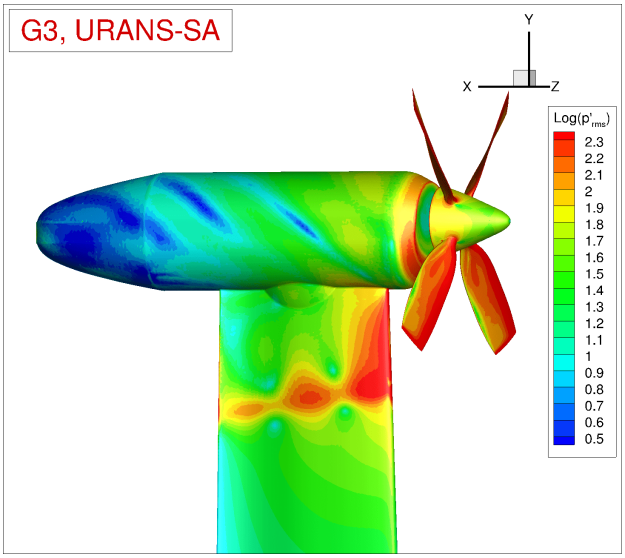

(b) URANS-SA Grid-03 A.

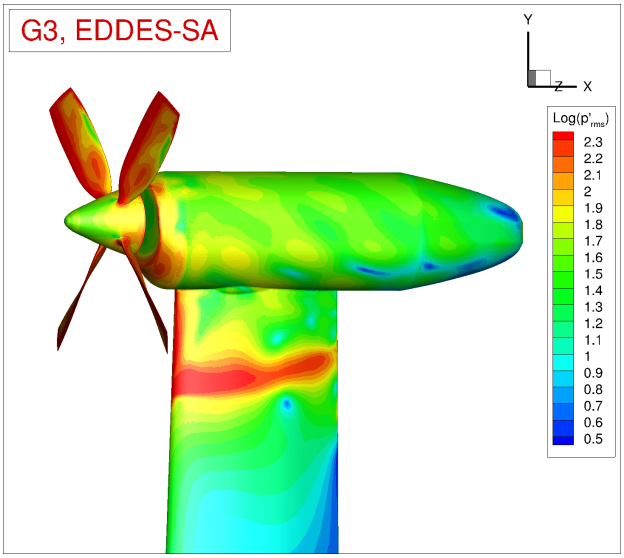

(c) EDDES-SA Grid-03 R.

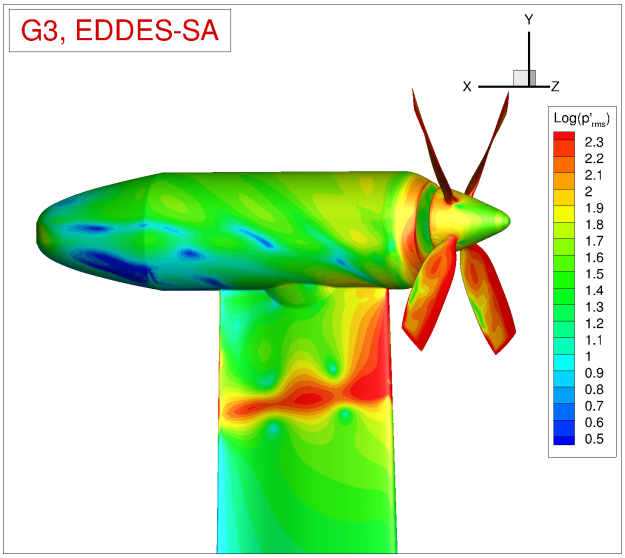

(d) EDDES-SA Grid-03 A.

Figure 6: The log of root-mean-square of pressure fluctuation computed by URANS-SA and EDDES-SA on Grid-03, $M_\infty = 0.11$, $C_T = 0.40$, $AoA = 0°$.

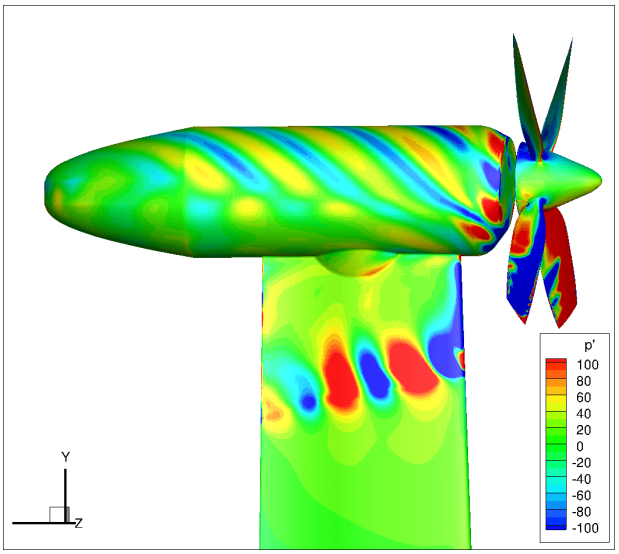

(a) $M_\infty = 0.08$, $AoA = 0°$

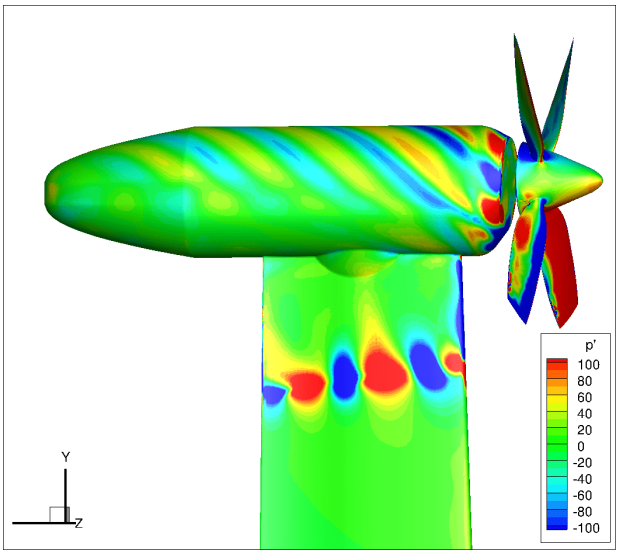

(b) $M_\infty = 0.11$, $AoA = 0°$

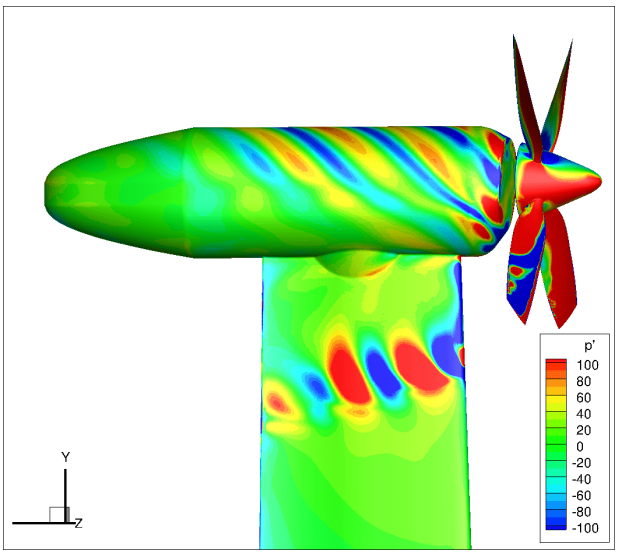

(c) $M_\infty = 0.08$, $AoA = 5°$

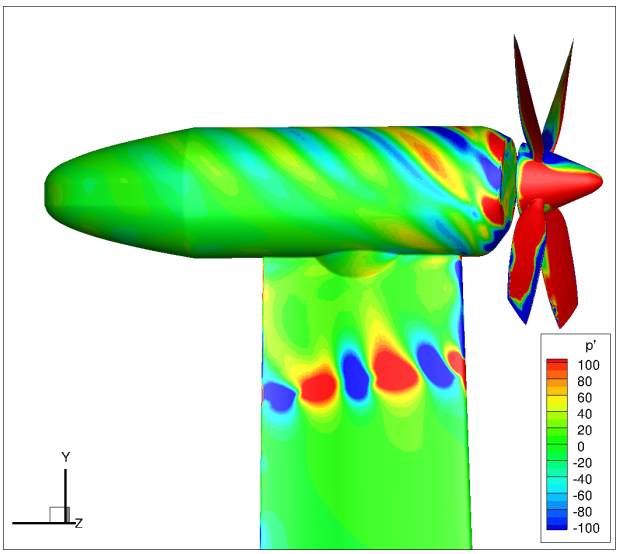

(d) $M_\infty = 0.11$, $AoA = 5°$

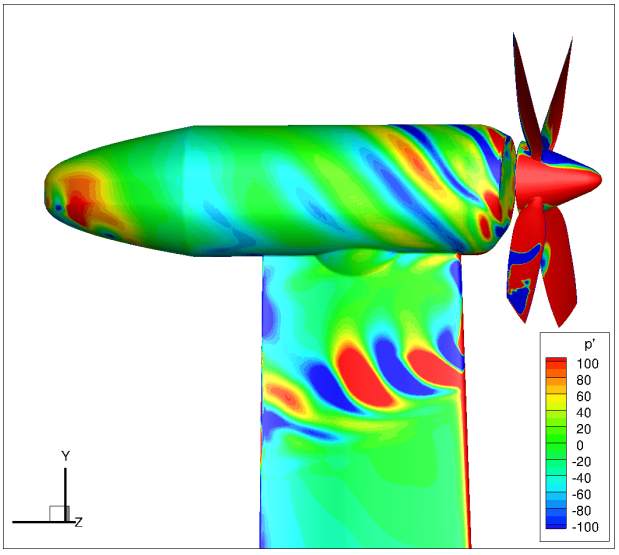

(e) $M_\infty = 0.08$, $AoA = 15°$

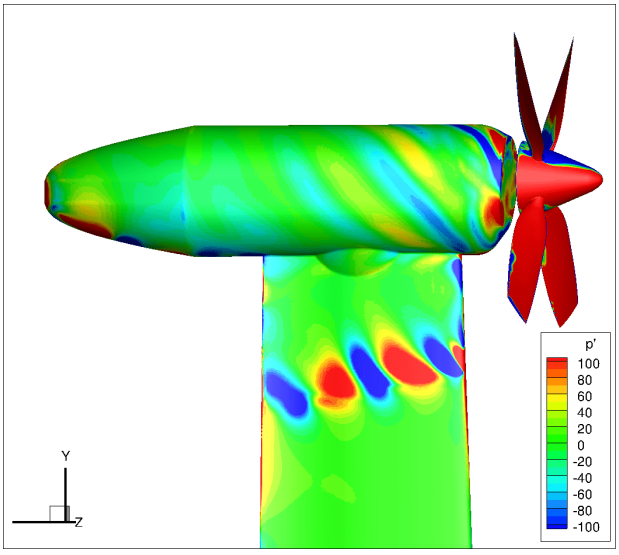

(f) $M_\infty = 0.11$, $AoA = 15°$

Figure 7: Instantaneous pressure fluctuation at $M_\infty = 0.08$ and 0.11 and $AoA = 0°, 5°$ and $15°$, viewed from the blade advancing side (below the propeller-wing assembly).

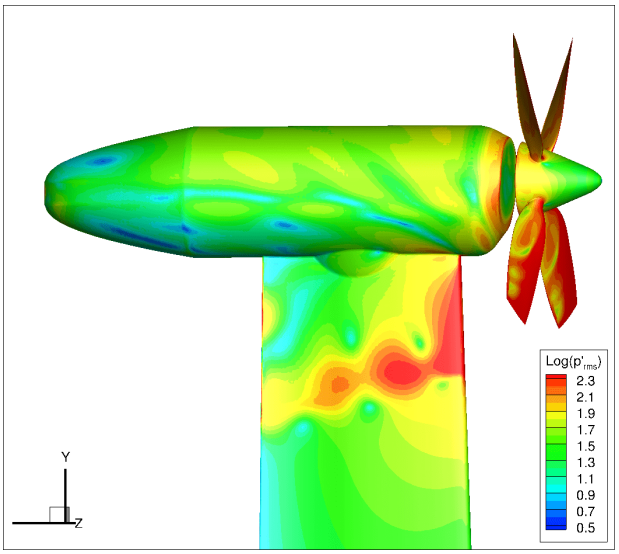

(a) $M_\infty = 0.08$, $AoA = 0°$

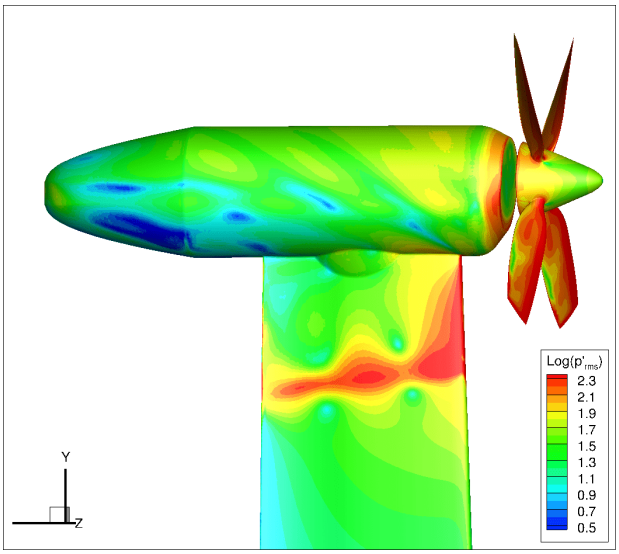

(b) $M_\infty = 0.11$, $AoA = 0°$

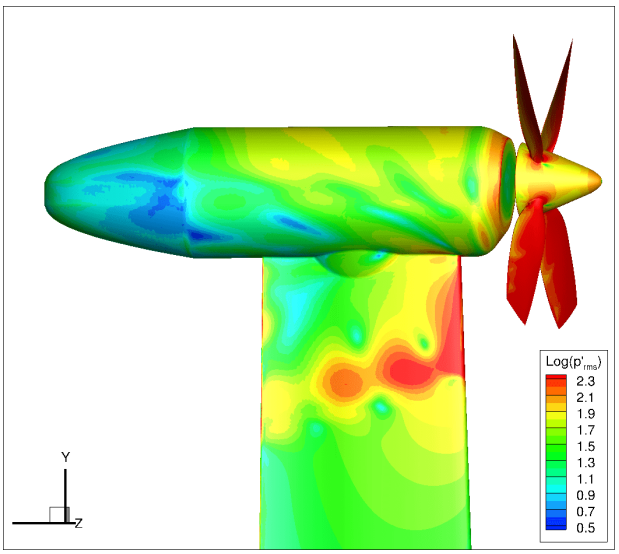

(c) $M_\infty = 0.08$, $AoA = 5°$

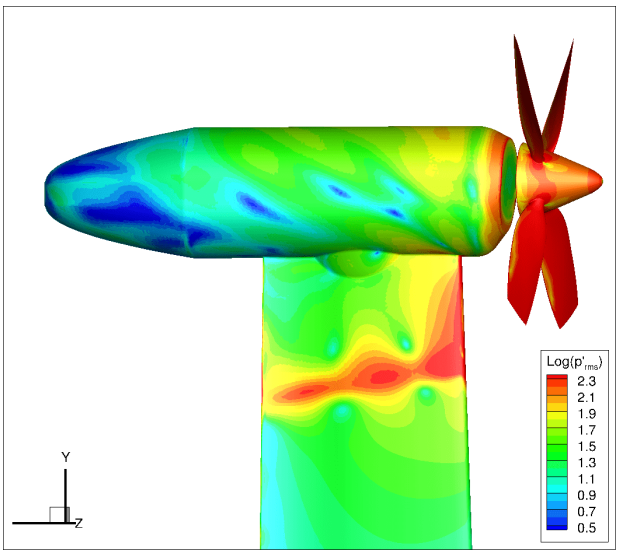

(d) $M_\infty = 0.11$, $AoA = 5°$

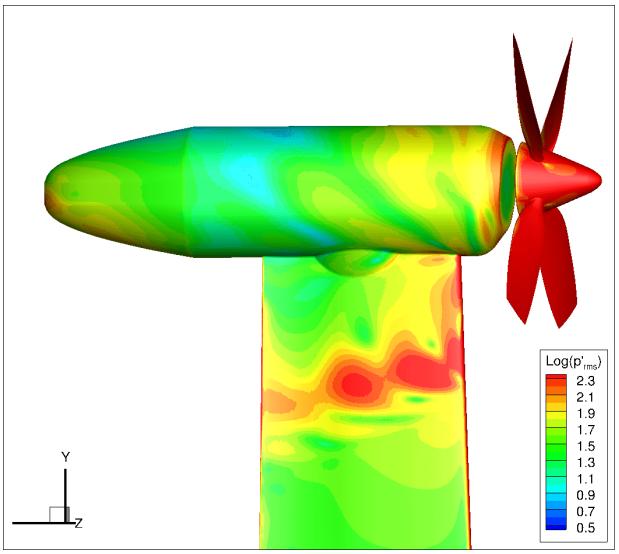

(e) $M_\infty = 0.08$, $AoA = 15°$

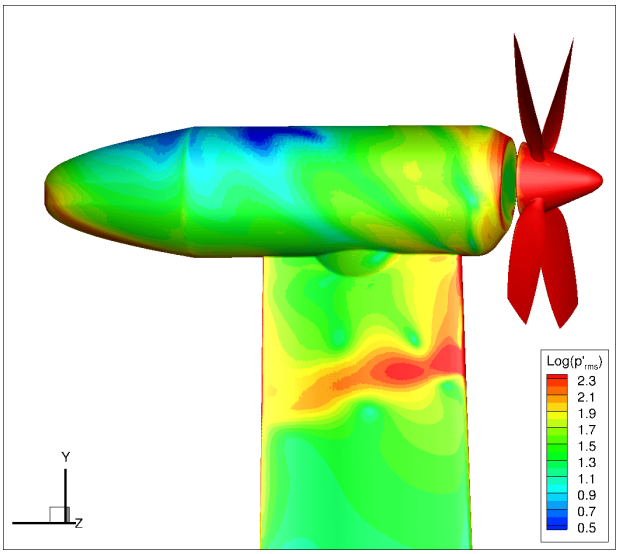

(f) $M_\infty = 0.11$, $AoA = 15°$

Figure 8: The log of root-mean-square of pressure fluctuation at $M_\infty = 0.08$ and 0.11 and $AoA = 0°, 5°$ and $15°$, viewed from the blade advancing side (below the propeller-wing assembly).

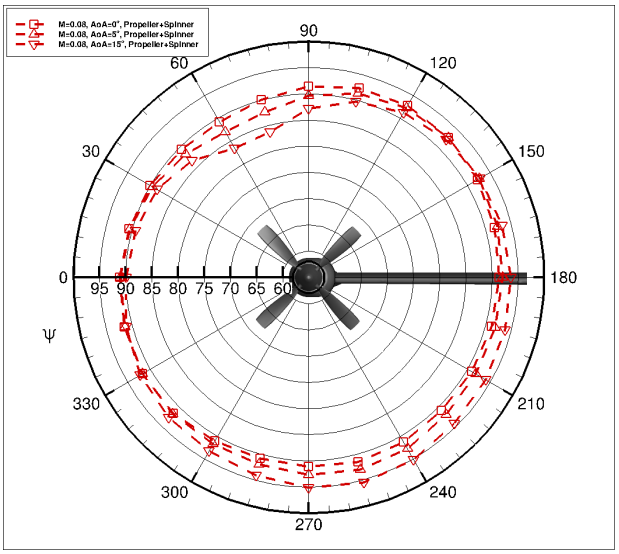

(a) $M_\infty = 0.08$, Propeller-Spinner Contribution

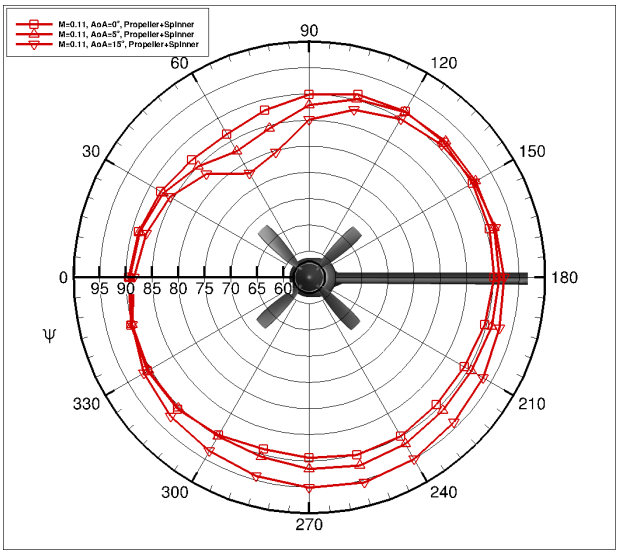

(b) $M_\infty = 0.11$, Propeller-Spinner Contribution

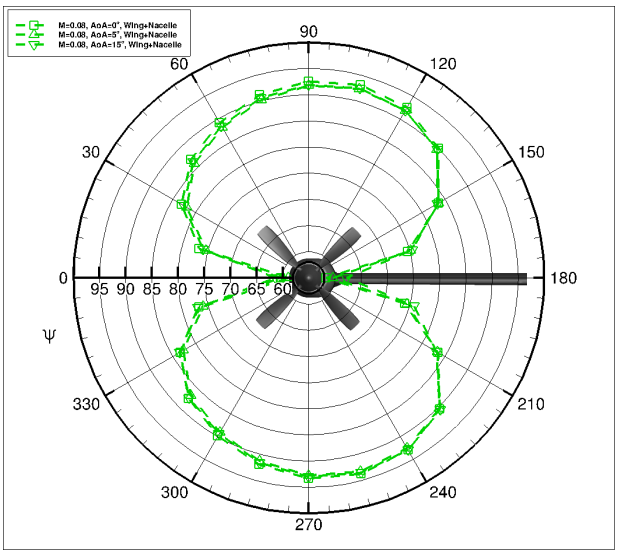

(c) $M_\infty = 0.08$, Wing-Nacelle Contribution

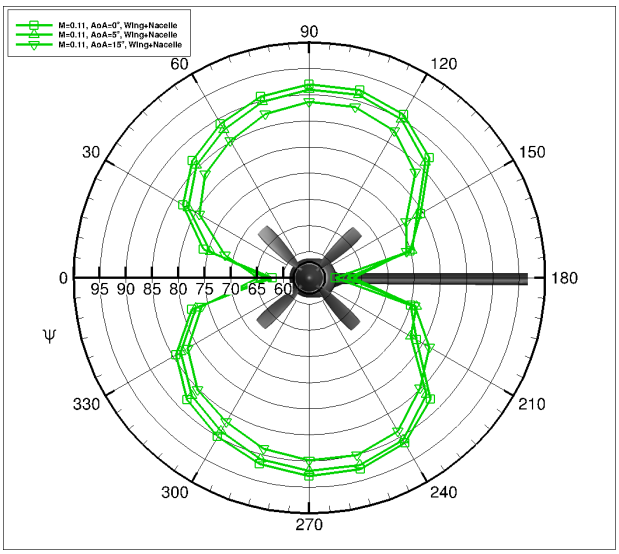

(d) $M_\infty = 0.11$, Wing-Nacelle Contribution

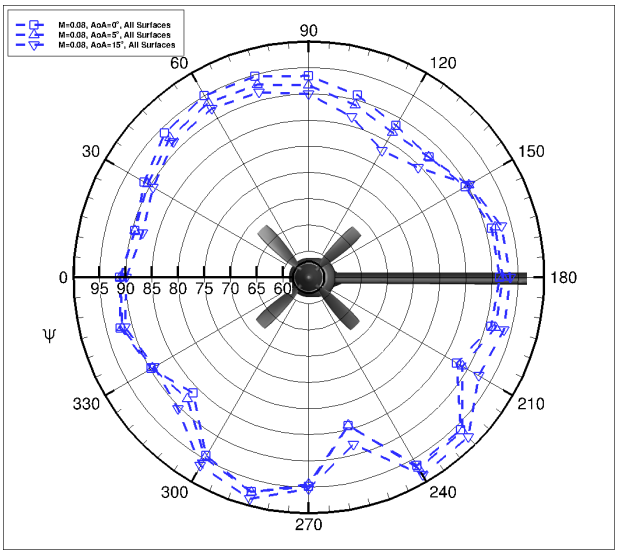

(e) $M_\infty = 0.08$, All Surfaces

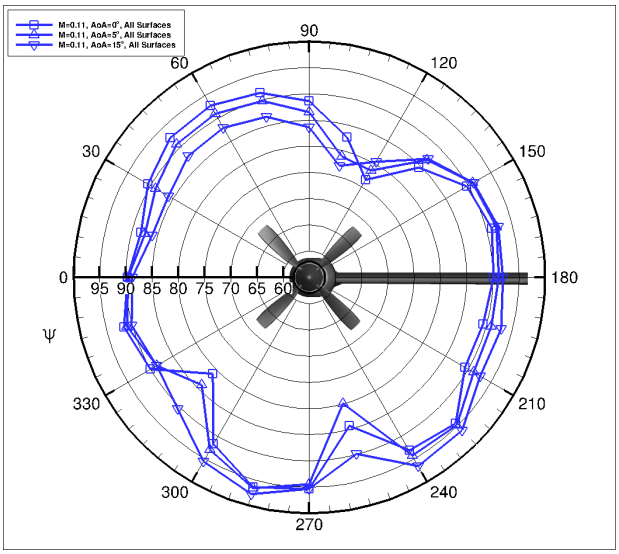

(f) $M_\infty = 0.11$, All Surfaces

Figure 9: Overall sound pressure level (OASPL) on the propeller azimuthal plane, showing contributions from propeller-spinner and wing-nacelle surfaces at $M_\infty = 0.08$ and $M_\infty = 0.11$.

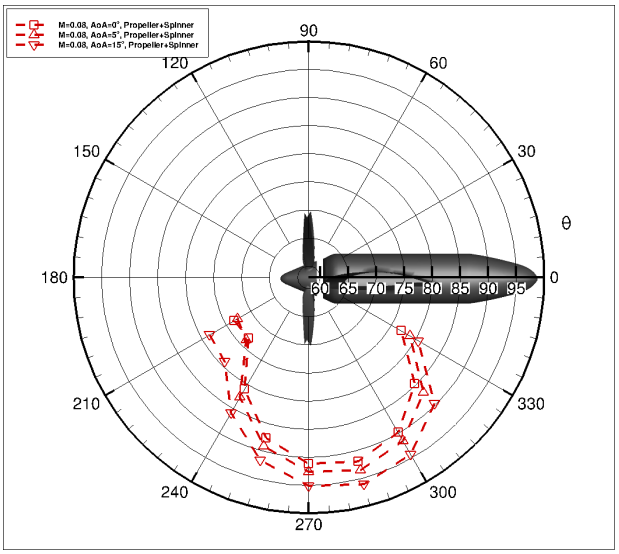

(a) $M_\infty = 0.08$, Propeller-Spinner Contribution

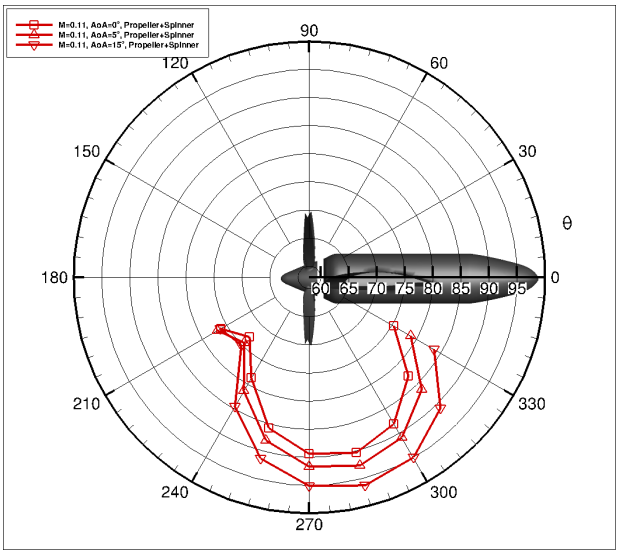

(b) $M_\infty = 0.11$, Propeller-Spinner Contribution

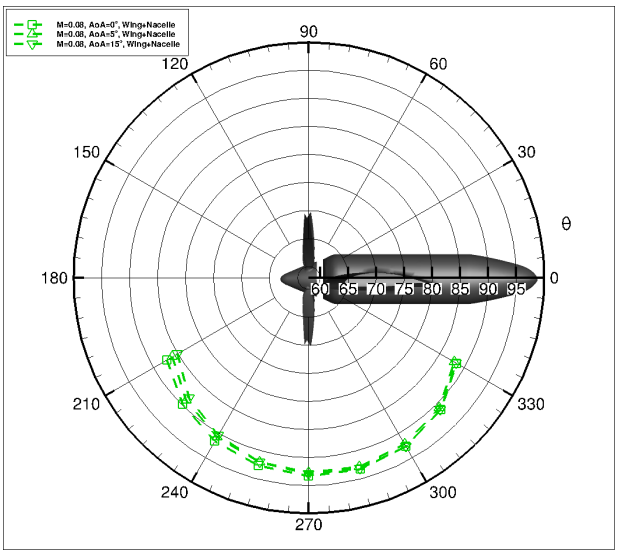

(c) $M_\infty = 0.08$, Wing-Nacelle Contribution

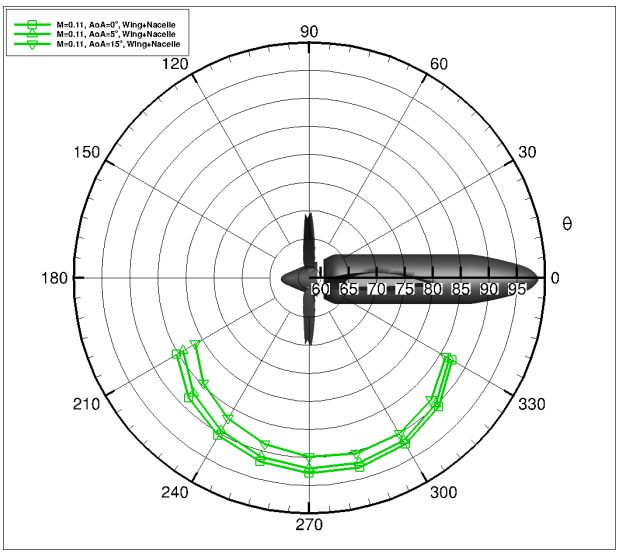

(d) $M_\infty = 0.11$, Wing-Nacelle Contribution

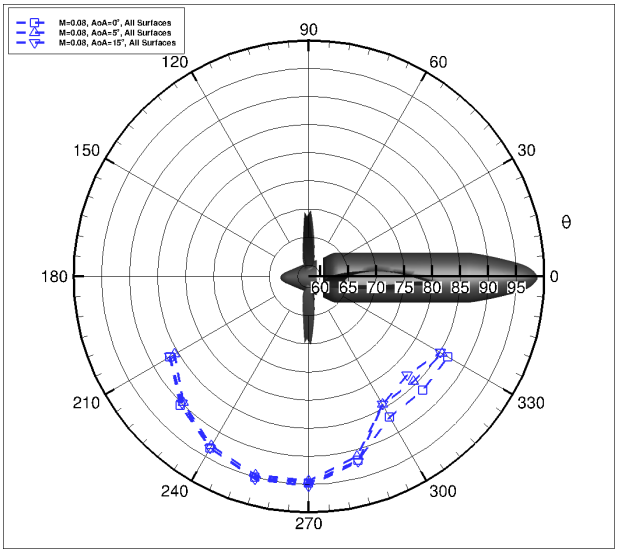

(e) $M_\infty = 0.08$, All Surfaces

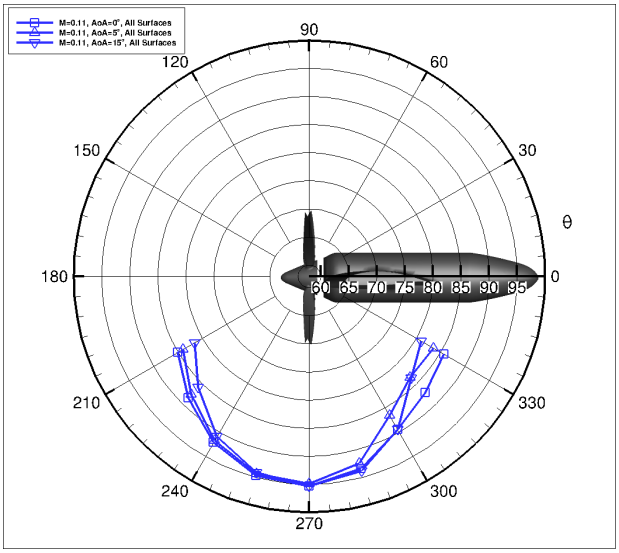

(f) $M_\infty = 0.11$, All Surfaces

Figure 10: Overall sound pressure level (OASPL) on the fly-over plane, showing contributions from propeller-spinner and wing-nacelle surfaces at $M_\infty = 0.08$ and $M_\infty = 0.11$.

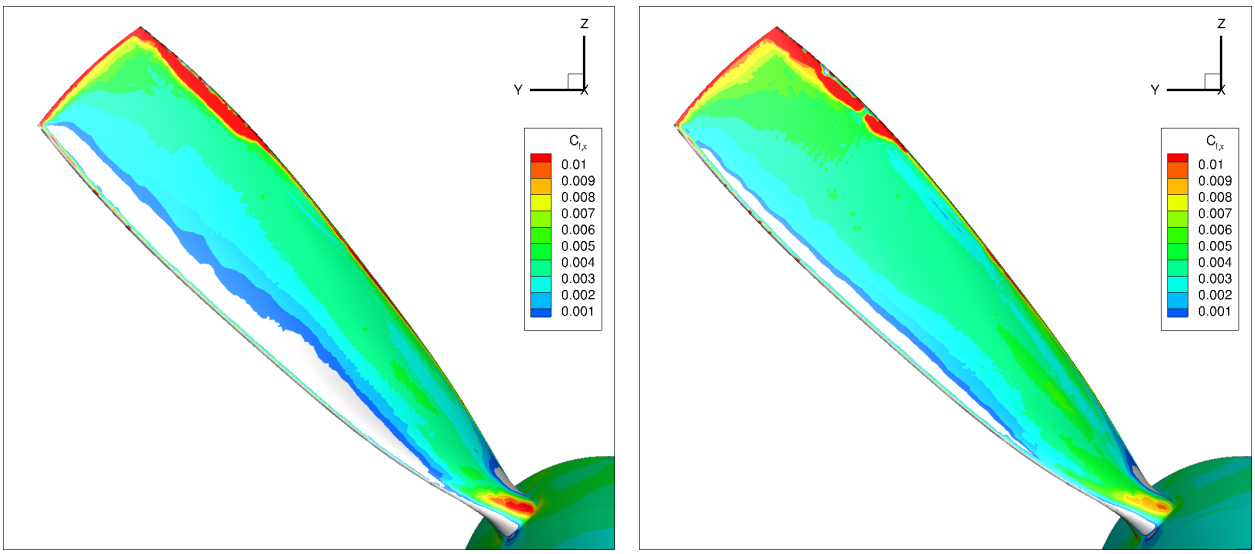

(a) $M_\infty = 0.08$, $AoA = 0^\circ$ (b) $M_\infty = 0.11$, $AoA = 0^\circ$

Figure 11: Wall shear stress distribution on the windward side of a blade at $M_\infty = 0.08$ and 0.11. The negative values are cut off to highlight the separated regions located towards the propeller leading-edge.

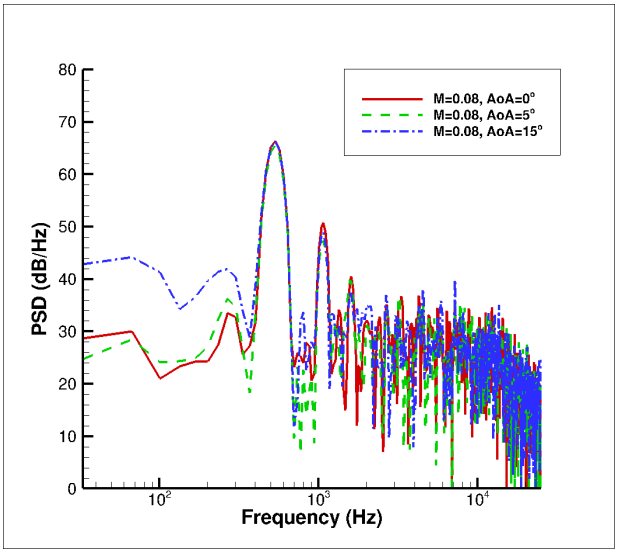

(a) $M_\infty = 0.08$, $\theta = 210°$

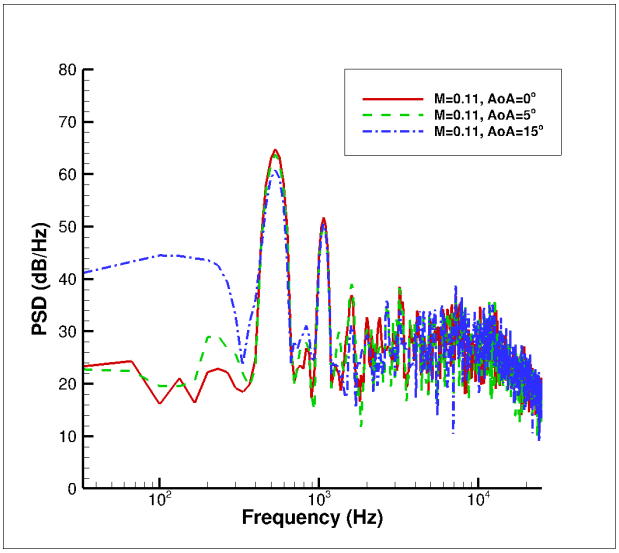

(b) $M_\infty = 0.11$, $\theta = 210°$

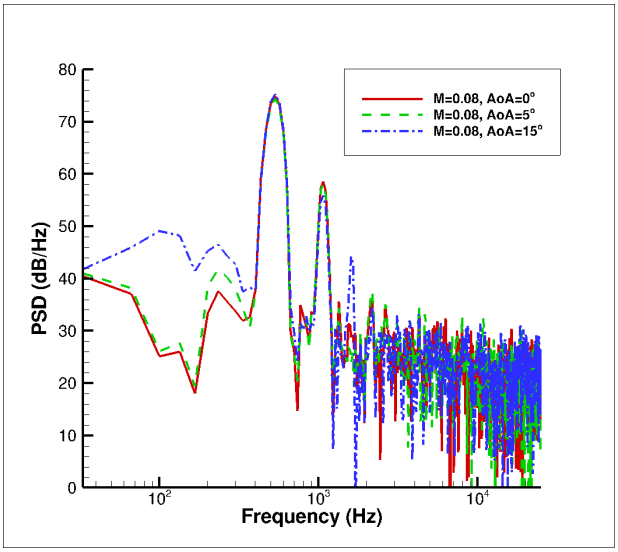

(c) $M_\infty = 0.08$, $\theta = 270°$

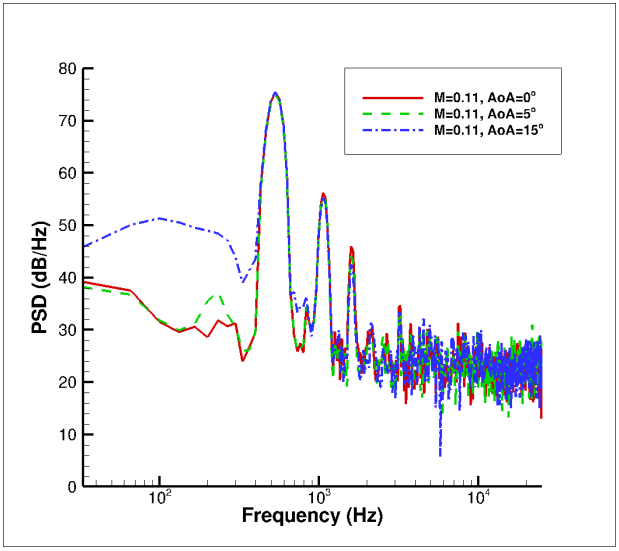

(d) $M_\infty = 0.11$, $\theta = 270°$

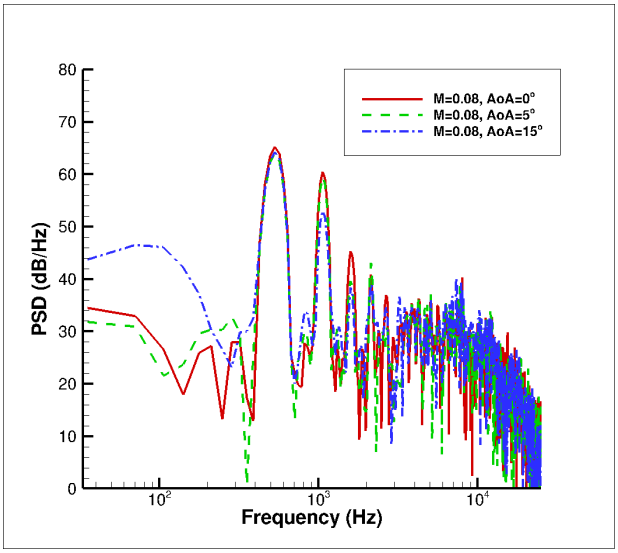

(e) $M_\infty = 0.08$, $\theta = 330°$

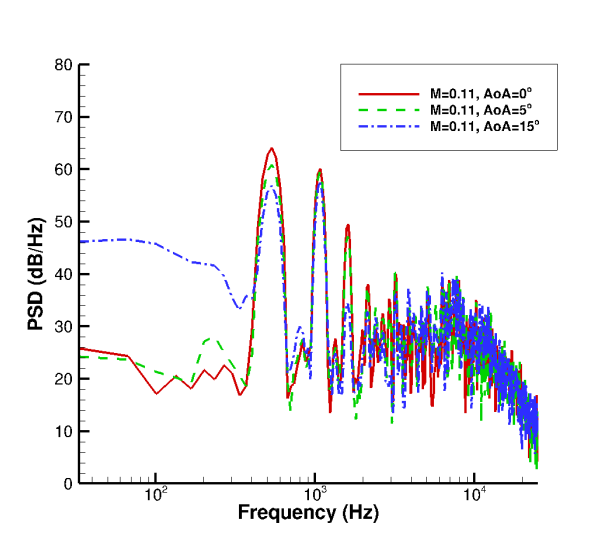

(f) $M_\infty = 0.11$, $\theta = 330°$

Figure 12: Noise power spectral density at three observer angles on the fly-over plane for $M_\infty = 0.08$ and $M_\infty = 0.11$.